


# The Thermodynamic Structure of Arctic Coastal Fog Occurring During the Melt Season over East Greenland

Gaëlle F. Gilson<sup>1</sup>  · Hester Jiskoot<sup>1</sup> · John J. Cassano<sup>2,3</sup> · Ismail Gultepe<sup>4</sup> · Timothy D. James<sup>5</sup>

Received: 16 June 2017 / Accepted: 3 May 2018 / Published online: 17 May 2018  
© Springer Science+Business Media B.V., part of Springer Nature 2018

**Abstract** An automated method to classify Arctic fog into distinct thermodynamic profiles using historic in-situ surface and upper-air observations is presented. This classification is applied to low-resolution Integrated Global Radiosonde Archive (IGRA) soundings and high-resolution Arctic Summer Cloud Ocean Study (ASCOS) soundings in low- and high-Arctic coastal and pack-ice environments. Results allow investigation of fog macrophysical properties and processes in coastal East Greenland during melt seasons 1980–2012. Integrated with fog observations from three synoptic weather stations, 422 IGRA soundings are classified into six fog thermodynamic types based on surface saturation ratio, type of temperature inversion, fog-top height relative to inversion-base height and stability using the virtual potential temperature gradient. Between 65–80% of fog observations occur with a low-level inversion, and statically neutral or unstable surface layers occur frequently. Thermodynamic classification is sensitive to the assigned dew-point depression threshold, but categorization is robust. Despite differences in the vertical resolution of radiosonde observations, IGRA and ASCOS soundings yield the same six fog classes, with fog-class distribution varying with latitude and environmental conditions. High-Arctic fog frequently resides within an elevated inversion layer, whereas low-Arctic fog is more often restricted to the mixed layer. Using supplementary time-lapse images, ASCOS microwave radiometer retrievals and air mass back-trajectories, we hypothesize that the thermodynamic classes represent different stages of advection fog formation, development, and dissipation, including stratus-base lowering and fog lifting.

---

✉ Gaëlle F. Gilson  
gaelle.gilson@uleth.ca

<sup>1</sup> Department of Geography, University of Lethbridge, Lethbridge, AB T1K 3M4, Canada

<sup>2</sup> Cooperative Institute for Research in Environmental Sciences, University of Colorado, Boulder, CO 80309, USA

<sup>3</sup> Department of Atmospheric and Oceanic Sciences, University of Colorado, Boulder, CO 80309, USA

<sup>4</sup> Meteorological Research Division, Environment and Climate Change Canada, Toronto, ON M3H 5T4, Canada

<sup>5</sup> Department of Geography, Queen's University, Kingston, ON, Canada

This automated extraction of thermodynamic boundary-layer and inversion structure can be applied to radiosonde observations worldwide to better evaluate fog conditions that affect transportation and lead to improvements in numerical models.

**Keywords** Arctic fog · Fog development · Greenland · Radiosonde observations · Temperature inversion

## 1 Introduction

Low-level clouds and fog are ubiquitous throughout the Arctic melt season, significantly influencing the surface energy budget including that of the cryosphere (Curry et al. 1996; Van Tricht et al. 2016). Clouds both cool the surface by reducing the amount of incoming shortwave radiation and warm the surface by increasing the downward longwave radiation (Nardino and Georgiadis 2003; Shupe and Intrieri 2004). The net result is usually a warming effect at the surface (Zhang et al. 1996; Serreze and Barry 2011; Bennartz et al. 2013), except for a few weeks in summer when surface albedo is low and solar elevation angle high (Curry et al. 1988; Shupe and Intrieri 2004). The influence of fog (which reduces horizontal visibility < 1 km: National Oceanic and Atmospheric Administration (NOAA) 1995) on the surface energy budget is also complex, and depends on the thermodynamic structure, microphysical properties and concurrent temperature inversion and cloud cover. Fog and low-level temperature inversions can decrease glacier ablation (Alt 1979; Braun et al. 2004; Koerner 2005; Mernild et al. 2008; Hulth et al. 2010), but have also been correlated with episodes of intensified sea-ice and glacier melt (Gardner and Sharp 2007; Chutko and Lamoureux 2009; Tjernström et al. 2015). Despite extensive research on Arctic clouds (Curry et al. 1996; Vavrus et al. 2011; Tjernström et al. 2012; Van Tricht et al. 2016), few have focused on Arctic fog (e.g. Nilsson and Bigg 1996; Hanesiak and Wang 2005; Heintzenberg et al. 2006; Gultepe et al. 2014). Fog and other boundary-layer clouds are still considered difficult to predict and remain a significant uncertainty in climate modelling (IPCC 2013). Fog research is also important for improved weather and visibility forecasting, which aids in the mitigation of transportation hazards (Bendix 1995; Gultepe et al. 2007). Over polar oceans, fog and low-cloud cover are expected to increase in frequency due to warmer oceans and the declining extent of seasonal sea-ice, but regional patterns of change remain uncertain (Deser et al. 2010; Eastman and Warren 2010; Palm et al. 2010; Vavrus et al. 2011; Liu et al. 2012).

Fog is most frequent in the Arctic melt season, with sea-fog being the most common type (Nilsson and Bigg 1996; Cappelen et al. 2001; Svendsen et al. 2002; Hanesiak and Wang 2005; Tjernström et al. 2012). Sea-fog can originate from the advection of a warm and moist air mass over a cold surface or by the subsidence of low-level clouds (Cotton and Anthes 1989; Koračin et al. 2001; American Meteorological Society 2015; World Meteorological Organization 2017). Arctic sea-fog peaks when sea-ice breaks up because the open water provides both moisture and heat fluxes to the boundary layer while remaining sea-ice offers a cooling surface. The presence of sea breezes may advect the fog up to tens of kilometres inland before it dissipates (Alt 1979; Cappelen 2015). Under clear-sky conditions, overnight longwave radiative cooling favours fog development, while after sunrise, shortwave heating exceeds longwave cooling and the mixing of warm dry air from aloft into the fog layer evaporates the fog droplets. This mixing can eventually penetrate the entire fog layer and lead to its dissipation providing relative humidity is decreased sufficiently (e.g. Gultepe et al.

2016). Dissipation can also occur through fog lifting into a low-level stratus cloud due to increased mechanical or thermal turbulence (Cotton and Anthes 1989; Koraćin et al. 2001). Conversely, air subsidence can favour fog formation through the establishment of a temperature inversion from adiabatic warming of the subsiding air, and through the presence of a humidity inversion (Telford and Chai 1984; Curry et al. 1988). Synoptic-scale anticyclones can, therefore, enhance fog formation through the lowering of an entire cold stratus deck (Koraćin et al. 2001), but a high rate of subsidence can accelerate fog dissipation because the dry and warm subsiding air causes the fog droplets to evaporate (Roach et al. 1982).

Fog and low-level stratiform clouds are usually associated with a stable boundary layer and frequently occur in the presence of a temperature inversion (Oke 1987). Temperature inversions occur in over 80% of Arctic summer soundings (Kahl 1990; Devasthale et al. 2010) and, while not a prerequisite for fog formation, they promote the development and maintenance of fog (Telford and Chai 1984; Cotton and Anthes 1989; Croft et al. 1997). Because Arctic sea-fog forms over a cold surface, after which the fog may advect over land and penetrate into warmer continental air, it often displays a thermodynamic structure with a surface-based inversion (Pilić et al. 1979; Leipper 1994; Lewis et al. 2003; Huang et al. 2015). As fog grows vertically, radiative cooling at its top generates instability and turbulence within the fog layer, which may result in a transition from a surface-based to a low-level inversion (Cotton and Anthes 1989; Sotiropoulou et al. 2014; Kim and Yum 2017). Mature fogs, therefore, often coincide with low-level elevated inversions (Leipper 1994; Zhang et al. 2009; Huang et al. 2015). Fog can also form through lowering of a stratus base and subsequent increase of relative humidity in the mixed layer below the inversion base (Pilić et al. 1979; Leipper 1994). Few studies have systematically investigated the thermodynamic structure of Arctic clouds in relation to temperature inversions using upper-air measurements. Sedlar and Tjernström (2009) classified Arctic stratocumulus clouds with respect to inversion-base height and identified two cloud regimes with distinct microphysical and radiative properties: (1) optically-thick and liquid-bearing clouds capped by the inversion base, and (2) mixed-phase clouds penetrating into deep and strong inversions, characterized by a smaller optical thickness and a longer lifetime. Similar thermodynamic structures have been observed for Arctic fog, where the fog-top extended above the inversion base (Sotiropoulou et al. 2016). None of these studies used long-term or low-resolution upper-air measurements, systematically investigated the variability in the fog-top relative to the inversion layer or evaluated transition processes between the thermodynamic regimes.

The aim of the present study is to develop an automated classification of the thermodynamic structure of melt-season Arctic fog in relation to thermal inversions and air-parcel stability. Using only archived surface and upper-air observations, this classification is first applied to high-resolution radiosonde data from the Arctic Summer Cloud Ocean Study (ASCOS; Tjernström et al. 2014), and subsequently to lower-resolution radiosonde profiles from the Integrated Global Radiosonde Archive (IGRA) measured twice-daily at three East Greenland stations over the period 1980–2012. Supported by the analysis of time-lapse images and airmass back-trajectories, we argue that the classification improves our understanding of the formation, development, and dissipation of liquid-phase Arctic coastal fog. Our results also help to assess how future changes in sea-ice and poleward advection of moisture and heat may affect fog occurrence. The thermodynamic classification presented here is applicable to any polar radiosonde station. The subsequent investigation of fog processes and macrophysical properties will aid in improving fog parametrization in weather forecast models for these regions.

## 2 Study Sites and Observations

### 2.1 Study Area

One region with a particularly high fog frequency is coastal East Greenland, where fog is present on average 20% of the time in July (Cappelen 2015). Along the East Greenland coast, three World Meteorological Organization (WMO) synoptic weather stations with concurrent radiosonde data were selected to cover a latitudinal range from low-Arctic to high-Arctic environments (Circumpolar Arctic Vegetation Map 2003). From north to south, these stations are Danmarkshavn (WMO identifier 4320, 11 m a.s.l., 76.77°N, 18.67°W), Ittoqqortoormiit formerly Scoresbysund (WMO identifier 4339, 70 m a.s.l., 70.48°N, 21.95°W) and Tasiilaq (WMO identifier 4360, 54 m a.s.l., 65.61°N, 37.64°W) (Fig. 1). Danmarkshavn and Ittoqqortoormiit stations are characterized by a 24-h daylight period during summer and sea-ice concentrations over 80% throughout the year due to the East Greenland Current transporting sea-ice south through the Fram Strait (Vinje 2001). The climate at Tasiilaq station is influenced by the proximity of the Icelandic Low and the warm Irminger Current (Hanna and Cappelen 2003; Cappelen 2015) and has a seasonal sea-ice cycle and more pronounced diurnal solar cycle. South-east Greenland is also more affected by katabatic flows, especially when the Icelandic Low is located between the East Greenland coast and Iceland (Klein and Heinemann 2002). In addition to weather and radiosonde observations at these three stations, time-lapse images near the Tasiilaq station and ASCOS data (Tjernström et al. 2014) from the *Oden* research icebreaker were used (Fig. 1). In summer, the local solar time at Danmarkshavn and Ittoqqortoormiit stations is UTC–1.5 h, and at Tasiilaq station it is UTC–2.5 h. All time indications used herein are given as UTC.

### 2.2 Data Observations and Instruments

We use a combination of ground and radiosonde data collected at three synoptic weather sites in East Greenland from 1980 through 2012. These datasets are complemented by a month of time-lapse images near Tasiilaq station to identify major fog physical processes, and observations from radiosondes with higher sampling rates collected in the central Arctic Ocean during an Arctic ship campaign (Fig. 1). The purpose of using this second dataset is to test the developed algorithm on high-resolution radiosondes profiles before applying the algorithm to the more widely-used lower-resolution radiosonde dataset. In addition, 500-hPa geopotential-level weather charts (<http://www1.wetter3.de/Archiv/>) and 120-h airmass back-trajectories from the NOAA HYSPLIT model (Stein et al. 2015) were analyzed to identify mesoscale and synoptic conditions during fog and evaluate airmass origin, in order to describe large-scale dynamical effects on Arctic sea-fog formation.

#### 2.2.1 Surface Weather Observations

Fog conditions were extracted from a combination of archived present weather and horizontal visibility observations provided by the Danish Meteorological Institute (DMI). Observations were made every three hours, starting at 0000 UTC. In the early 2000s, the sampling resolution switched to hourly observations, coincident with a change from manned to automated observations as reported in METAR (airport) and DMI files (Bødtker 2003). Present weather, ww, and horizontal visibility, vv, are reported as codes (WMO 1995: tables 4677, 4680 and

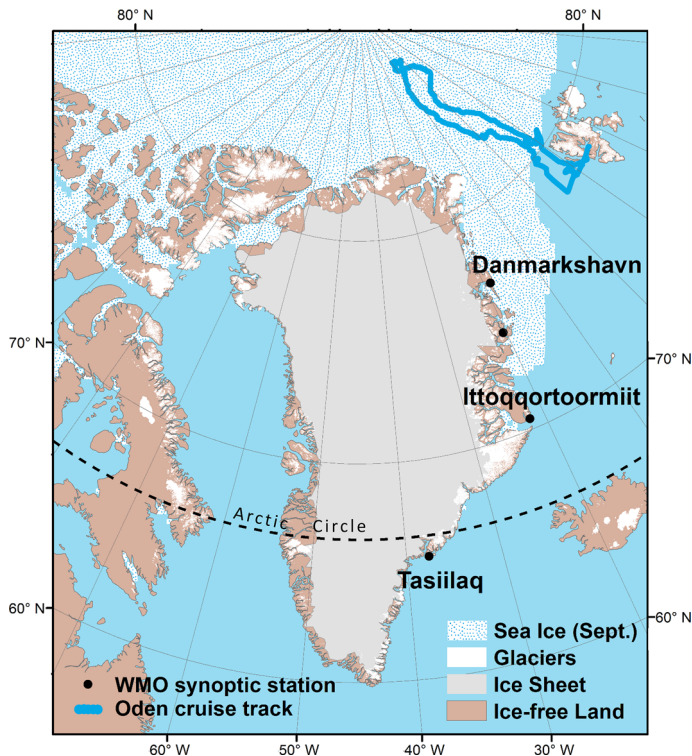


**Fig. 1** Locations of WMO synoptic weather stations with radiosonde observations along the East Greenland coastline (1980–2012) and of the *Oden* cruise track in the central Arctic Ocean during the ASCOS campaign (Aug–Sept 2008, Tjernström et al. 2014). The sea-ice limit represents the average minimum September extent (National Snow and Ice Data Center: <https://nsidc.org>, NSIDC-0051). The Greenland Ice Sheet was reconstructed from hydrologic outlets (NSIDC-0372, Lewis and Smith 2009) and peripheral glaciers from the Randolph Glacier Inventory (<http://www.glims.org/RGI/>, Pfeffer et al. 2014). The time-lapse camera was located 15 km to the north-west of Tasiilaq station; with a south-west oriented viewshed across Sermilik Fjord

4377). Current automated synoptic weather stations use the forward-scatter FD12P Vaisala Present Weather Sensor (Claus Nehring, pers. comm, May 2016), which has an accuracy of  $\pm 10\%$  for measurements of meteorological optical range (Vaisala 2002).

The majority (66–82%) of fog observations in East Greenland occur between May and August (Cappelen et al. 2001; Gueye 2014), coinciding with the Arctic melt season (Serreze et al. 2007). Our analysis is, therefore, restricted to warm fog, defined as liquid or supercooled fog with a temperature above  $-10\text{ }^{\circ}\text{C}$  (Petterssen 1956). Fog at a distance or in patches was excluded, as the fog might be missed by the radiosonde. One month of 30-min interval time-lapse images (downsampled to  $1800 \times 1200$  pixels) from Sermilik Fjord, 15 km north-west of Tasiilaq were used to complement weather and upper-air observations from the Tasiilaq station, with the main aim of determining fog type, and formation and dissipation processes. The 15.1 megapixel Canon EOS 50D 28-mm single-lens reflex camera was set up between 5 July and 5 August 2011 to overlook the 9-km-wide fjord mouth in a south-westward direction.

### 2.2.2 Upper-Air Observations

Historic radiosonde data for the three East Greenland synoptic WMO sites were acquired through the quality-controlled Integrated Global Radiosonde Archive (IGRA portal: <https://www.ncdc.noaa.gov/data-access/weather-balloon/integrated-global-radiosonde-archive>, Durre et al. 2006; Durre and Yin 2008). IGRA measurements used herein include pressure, geopotential height, dry-bulb temperature, dew-point depression, virtual potential temperature (gradient), and zonal and meridional wind components. Radiosonde balloons were launched twice daily, usually at about 1100 and 2300 UTC. IGRA profiles were reported at mandatory pressure levels (1000, 925, 850, 700, 500 hPa, etc.) as well as significant thermodynamic levels, in order to account for significant changes in temperature and humidity gradients between mandatory levels (Durre et al. 2006). All downloaded raw IGRA soundings have gone through user-input pre-processing in which some lower-level sonde measurements may have been adjusted using surface station data. In addition, although IGRA reports observations at a surface level, these are not always measured by the radiosonde and may be taken from a nearby weather station (Durre et al. 2006). All stations changed from radiosonde model RS18/21 to RS80 in the early 1980s (Gaffen 1993), with an increase in sonde accuracy (e.g. Antikainen et al. 2002). For this reason, and to minimize data and location inhomogeneities, our analysis was restricted to data from 1980 onwards. After this main sonde switch, there has been an alternate use of Vaisala sonde types RS80, RS90 and RS92, which have an accuracy of 1 hPa, 0.5 K, 5% (relative humidity) and 25 m (derived resolution for geopotential height). In order to account for data inaccuracies introduced by the pre-processing of the radiosonde data, the potential use of weather station data for the surface level, and instrument switches, a sensitivity analysis was conducted (see Sect. 5.3) to verify the robustness of the thermodynamic profile classification.

In addition to Greenland radiosondes, two upper-air datasets from the Arctic Summer Cloud Ocean Study (ASCOS: [www.ascos.se](http://www.ascos.se), Tjernström et al. 2014) aboard the Swedish ice-breaker *Oden* in the northern Greenland Sea and Arctic Ocean pack ice for August–September 2008, were used in this analysis (Fig. 1). The six-hourly 5-m reported vertical resolution Vaisala RS92 radiosondes were analyzed in combination with 5-min 7-m vertical resolution temperature profiles obtained from a 60-GHz scanning radiometer (near the surface; the vertical resolution decreases with height). Temperature retrievals from that microwave radiometer were found to be sufficiently accurate to be used in combination with radiosonde profiles (Sotiropoulou et al. 2014). The purpose of this analysis was to validate the interpretation of fog thermodynamic profiles from IGRA soundings and to determine the short-term evolution of the boundary layer.

## 3 Methods

Each radiosonde profile that was simultaneous with a fog event reported in the present weather data (ww) of the DMI synoptic station was extracted. Additionally, radiosonde launches occurring 2 h after and 1 h before two consecutive fog present weather observations were analyzed since it was assumed that fog persisted over this entire 3-h time interval. Hereafter, these long-duration fog events are referred to as non-simultaneous sounding observations. Total numbers of melt season (May–August) fog soundings, simultaneous and non-simultaneous with surface weather observations, are reported in Table 1. Non-simultaneous soundings represent the majority of extracted radiosonde fog profiles over Ittoqqortoormiit and Tasiilaq



**Table 1** Total number of soundings and fog soundings in the melt seasons (May–August) of 1980–2012

	Danmarkshavn		Ittoqqortoormiit		Tasiilaq	
	All	≥ 5 levels	All	≥ 5 levels	All	≥ 5 levels
All melt-season soundings	6745		6556		7013	
Total fog	236	[187]	152	[121]	149	[114]
Simultaneous	103	[99]	41	[39]	35	[28]
Non-simultaneous	133	[88]	111	[82]	114	[86]
Fog frequency (%)		[3.5]		[2.3]		[2.1]

Simultaneous refers to soundings occurring at the same time as surface weather observations, and non-simultaneous to those in between two consecutive surface weather observations. Numbers in brackets exclude missing soundings (majority of exclusions), soundings with surface temperature  $< -10$  °C (Petterssen 1956), and soundings with fewer than five levels below the 700-hPa pressure level in either the dry-bulb temperature or the dew-point depression profiles (after Kahl et al. 1992). Fog frequency is the percentage of all melt-season soundings retained for fog analysis

stations, occurring 68 and 75% of the time, respectively. After the year 2000, more soundings coincided with the timing of synoptic fog observations because of the increased sampling rate in ground observations. Only radiosondes with a minimum of five levels between the surface and the 700-hPa pressure level in both the dry-bulb temperature and dew-point depression profiles were included in this analysis (Table 1, numbers in brackets). Fewer levels may either result in a correct but smooth profile or in an unreliable sounding. Since Kahl et al. (1992) determined five levels to be a minimum to study low-level inversion properties, it was decided to use this strict threshold, with the risk of excluding several reliable smooth soundings. This resulted in the exclusion of 19 soundings ( $< 5\%$  of all soundings).

Each radiosonde profile was analyzed for saturation gradient, temperature inversion type, stability, and approximation of fog-top height with respect to the inversion base. The radiosonde data were used to obtain the following parameters:

- Dew-point depression ( $T_{dd} = T - T_d$ , where  $T$  is the dry-bulb air temperature and  $T_d$  is the dew-point temperature) profiles were used to calculate air parcel saturation. A  $T_{dd}$  value for saturation was determined from the lowest tropospheric level of the 166 soundings coinciding with fog observations (Table 1) and this was defined as the surface dew-point depression  $T_{dds}$ . A  $T_{dds}$  threshold of 1 °C, commonly used in the literature (e.g. Meyer and Rao 1999; Kim and Yum 2010; Koračin et al. 2014), captured almost 100% of fog observations at Danmarkshavn and Tasiilaq stations, and about 75% at the Ittoqqortoormiit station (Fig. 2). Despite having to exclude approximately one quarter of potential fog soundings at the Ittoqqortoormiit station (most likely due to a combination of environmental conditions and instrument differences), a fixed  $T_{dds} = 1$  °C threshold was used for all stations and applied throughout the entire  $T_{dd}$  profiles. This threshold corresponds to relative humidity ( $RH$ ) with respect to liquid water  $RH_w > 93\%$  (Hardy 1998) and corresponds to  $RH_w$  values recorded in IGRA soundings during warm fog in our study region. The fog-top height was assigned the radiosonde-derived geopotential height corresponding to the location where  $T_{dd}$  first exceeds the saturation threshold  $T_{dds}$ .
- Dry-bulb temperature ( $T$ ) was used to classify the inversion type. The height of the inversion base above sea level was determined from the geopotential height; surface-based inversions (positive temperature gradient from the ground surface up) were separated from low-level inversions (elevated inversion base below the 700-hPa pressure level (Kahl

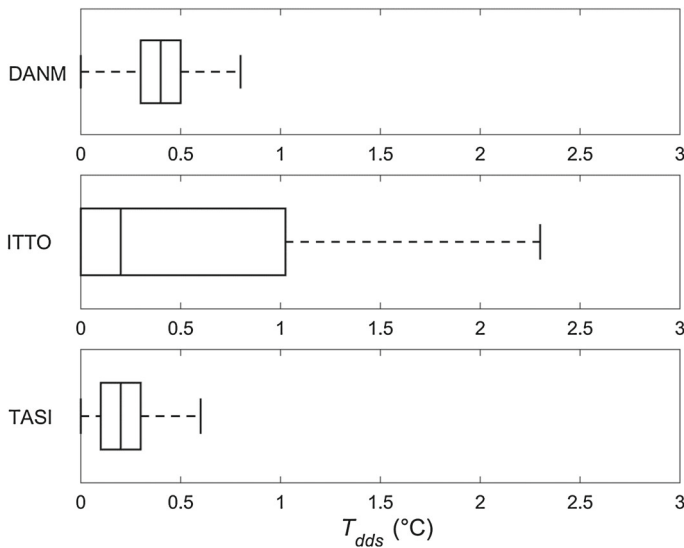


**Fig. 2** Surface dew-point depression ( $T_{dds}$ ) statistics during fog from surface level of soundings simultaneous with fog observations at the nearby weather station (1980–2012). Box-and-whisker plots show the median (vertical line), lower and upper quartiles (left and right edge of box), and 5th and 95th percentiles (range)

et al. 1992)). By extension, the term “low level” is used herein to refer to the atmosphere above the surface but below the 700-hPa level.

- The virtual potential temperature ( $\Theta_v$ ) gradient ( $\mu = d\Theta_v/dz$ ) was used to determine air-parcel stability. A saturated air parcel at the surface is statically stable (unstable) if  $\mu$  is positive (negative), or neutral if zero (Stull 1988). For this analysis, neutral lapse rates were regarded as unstable lapse rates, and the stability of the surface layer,  $\mu_s$ , was defined as the stability of the air parcel delimited by the surface level and the next level aloft. By extension, the term surface layer is used to refer to the air parcel delimited by the first two sounding levels. Even though other studies have used the equivalent potential temperature to describe the stability of the boundary layer (e.g. Sedlar et al. 2012; Shupe et al. 2013; Sotiropoulou et al. 2014), choosing  $\Theta_v$  was motivated here by its availability in IGRA files; therefore, reducing the potential for introducing additional calculation errors, as well as to remain consistent with boundary-layer theory (Stull 1988) and previous studies on sea-fog turbulence (Telford and Chai 1984; Nilsson 1996; Nakanishi and Niino 2006).

For each of the fog events captured by radiosonde (Table 1) a standardized graph was generated by combining panels of surface weather observations and upper-air profiles of  $T$ ,  $T_d$ , wind direction and specific humidity (not shown here). A skew-T log-P diagram was used to plot  $T$  and  $T_d$ , facilitating the initial identification of distinct thermodynamic profiles. Ultimately, all thermodynamic profiles were automatically classified into one of six distinctive fog sounding types, through a script developed for this purpose. This classification was based on their thermodynamic vertical profile differences in saturation gradient, temperature inversion type, stability, and approximation of fog-top height with respect to inversion base, as explained above. This automated thermodynamic characterization was inspired by the classification of stratiform clouds capped by a low-level inversion or residing inside a low-



level inversion by Sedlar and Tjernström (2009), who discriminated these two distinct types of clouds based on their physical, optical, and temporal properties.

The fog-sounding type classification was first performed on the 46 high-resolution radiosonde profiles with identified fog events from ASCOS soundings, in an attempt to validate the classification applied to IGRA data. The identification of fog events during the ASCOS campaign was derived from a subjective probability product (Tjernström et al. 2012), in which only observations with horizontal visibilities <5 km and ceilings <100 m above ground level (a.g.l.), or horizontal visibilities <1 km, or horizontal visibilities <2 km and ceilings <80 m a.g.l., and no concurrent precipitation with either one, were retained for the classification of fog. To determine saturation and classify the identified fog events, it was decided to apply two different  $T_{\text{dds}}$  thresholds: at 1 °C and at 0.5 °C. The second  $T_{\text{dds}}$  threshold was chosen because the radiosonde model Vaisala RS92 used during the ASCOS campaign (Tjernström et al. 2014) provides more accurate humidity measurements than the older models used at WMO synoptic stations (Antikainen et al. 2002; Steinbrecht et al. 2008; Vaisala 2017).

## 4 Results

### 4.1 Fog Thermodynamic Profiles

Using an automated characterization of each sounding, thermodynamic profiles from both ASCOS (Sect. 4.2) and IGRA (Sect. 4.3) radiosondes could be classified into six major fog classes as described in Fig. 3. Class 1 are excluded events because the dew-point depression threshold suggests there is no saturation in the radiosonde profile; Class 2 is fog with a surface-based inversion; Classes 3–5 are fog events with a low-level inversion, with the fog-top below (Class 3), at (Class 4) or above (Class 5) the low-level inversion base; and Class 6 has fog with an overlying saturated (stratus) layer within the low-level inversion. Class 2 exhibits some variability in humidity profiles (not shown), but the differences are small and there are too few observed cases to further subdivide Class 2. In addition, fog occasionally occurs without any inversion (stable layer with isothermal or positive temperature lapse rate profile), but these arise in <1% of IGRA fog observations at all stations and are, therefore, not considered further in the analysis.

### 4.2 Thermodynamic Profiles During the ASCOS Campaign

The proposed thermodynamic classification was first applied to 1 month of high-resolution radiosonde data from the ASCOS campaign, of which 46 fog soundings were identified. The relative frequencies of each fog class using the two  $T_{\text{dds}}$  thresholds are presented in Fig. 4, and typical profiles in Fig. 5. The vast majority of fog occurs with a low-level inversion, of which Class 5 is observed most frequently and is the most vertically extensive fog type. Transitions between Classes 5 (fog) and 1 (stratus) are common. Although Class 6 occurs in only 7–20% of all ASCOS fog observations (Fig. 4), at the onsets of fog lifting or stratus-base lowering (Fig. 5a), Class 6 occurs in >75% of the time. In these cases, fog was not reported in Fig. 4. Class 4 predominantly occurs in the dissipating stages of fog events (Fig. 5e), as does Class 3. Changing the  $T_{\text{dds}}$  threshold does not change the number of fog cases, but the  $T_{\text{dds}} = 0.5$  °C threshold results in more fog classified as Classes 1 and 6, and less Class 5.

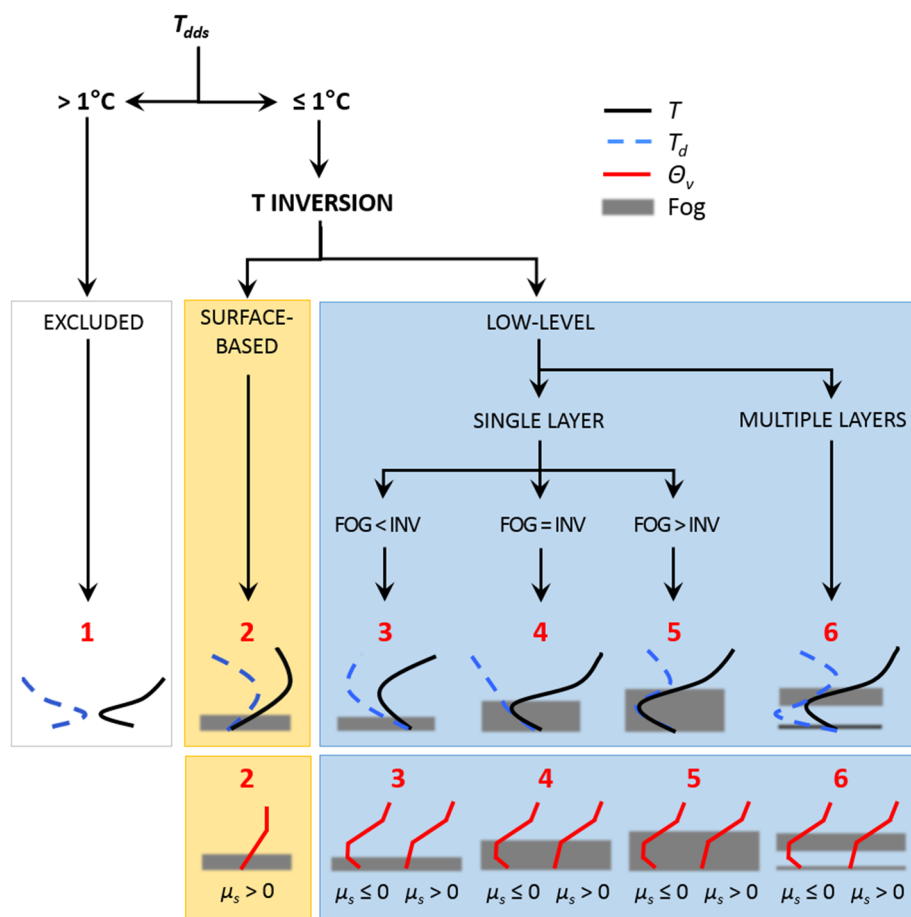


**Fig. 3** Six fog classes (red numbers) based on surface dew-point depression threshold ( $T_{dds}$ ), lower tropospheric inversion type, and fog-top height relative to the inversion base. White box: fog events not captured by radiosonde ( $T_{dds} > 1^\circ\text{C}$ ). Yellow boxes: fog with a surface-based inversion. Blue boxes: fog with a low-level inversion, described for fog-top below (<), coinciding with (=) or above (>) the inversion base (INV). Classes 2–5 have no significant low-level cloud layer above the fog, thus are classified as single layer cases. Class 6 corresponds to a thin fog layer overlain by a low stratus in a low-level inversion (multiple layers). Red lines are stability profiles for each class:  $\Theta_v$  is the virtual potential temperature and  $\mu_s$  the virtual potential temperature gradient at the surface ( $\mu_s \leq 0$ : unstable or neutrally stratified,  $\mu_s > 0$ : stably stratified)

Multiple low-level cloud layers are frequently observed based on ASCOS soundings (e.g. Fig. 5e, f).

Visual analysis of temperature profiles retrieved from the ASCOS microwave radiometer between the 6-h interval ASCOS radiosonde launches provided us with information on the short-term (5-min interval) evolution of the boundary layer during fog, or when fog was forming or dissipating. The following key observations on the relationship between Arctic fog and temperature inversions were made from the combination of these ASCOS radiosonde and microwave radiometer profiles:

- Fog usually requires a low-level or surface-based temperature inversion to form as opposed to that stated by Telford and Chai (1984);

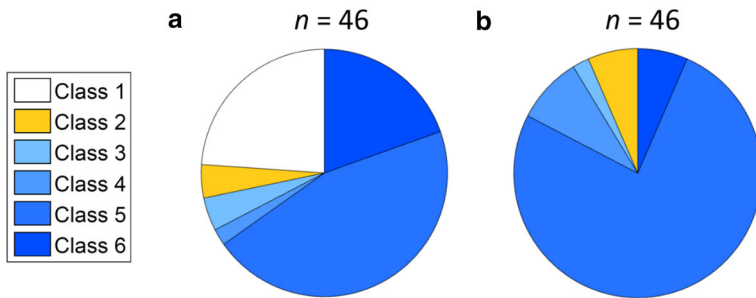


**Fig. 4** Fog class occurrence statistics from ASCOS soundings, for a surface dew-point depression threshold of **a** 0.5 °C and **b** 1 °C

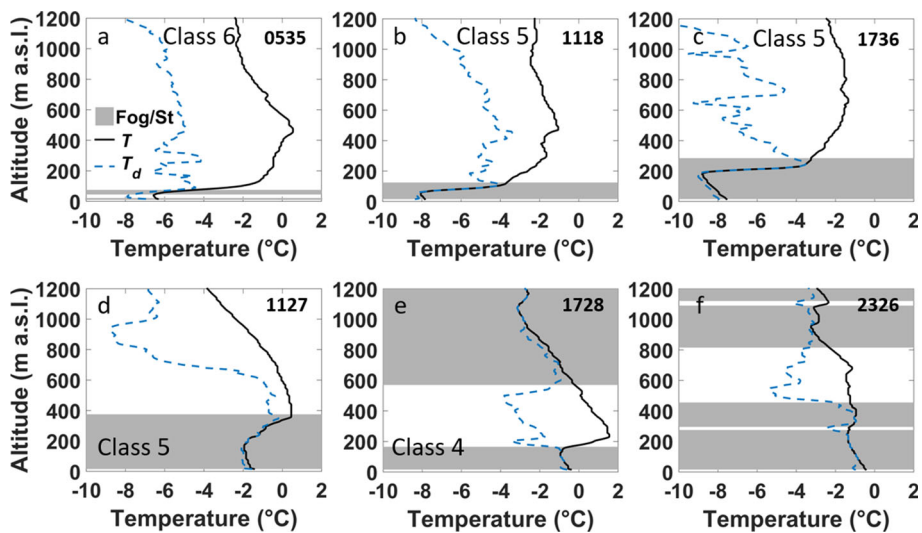


**Fig. 5** Examples of ASCOS radiosonde profiles during **a–c** fog formation (Classes 6 and 5; 22 August 2008), and **d–f** fog dissipation processes (Classes 5 and 4; 23 August 2008). Note that **f** is the transition of Class 5 to the inversion being eroded. The solid black line is the dry-bulb temperature  $T$ , the dashed blue line is the dew-point temperature  $T_d$ , and grey shadings represent fog and/or low stratus layers determined with  $T_{dds} \leq 1$  °C. Time (upper right corner) is given in UTC

- Erosion of the inversion (profile becoming isothermal, e.g. Figure 5f) often occurs during the dissipating stages of fog;
- Transitions between surface-based and low-level inversions are observed during fog.

### 4.3 Thermodynamic Profiles from IGRA Soundings

The same automated method used for the high-resolution ASCOS radiosonde profiles was then applied to IGRA lower-resolution radiosonde data over the three East Greenland locations for the summers of 1980–2012. A total of 422 IGRA soundings corresponding to fog conditions were analyzed. Occurrence statistics are reported in Fig. 6 and Table 2. Comparisons between stations were tested through Chi square statistical tests ( $\chi^2$ ), while statistics

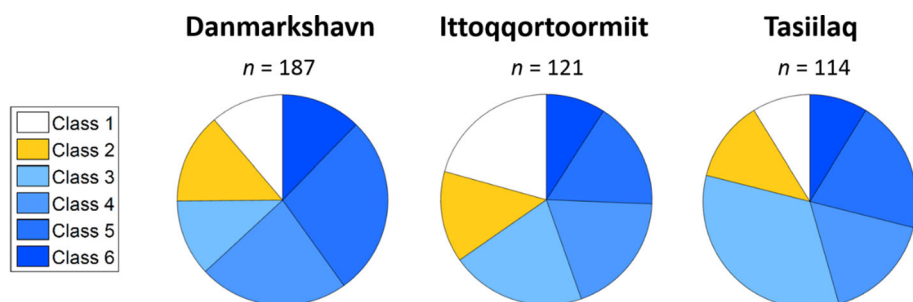


**Fig. 6** Fog occurrence statistics representing Danmarkshavn, Ittoqqortoormiit and Tasiilaq stations. See Table 2 for details

for each single station were tested through binomial tests at the 95% confidence interval. Results for class frequencies are displayed in Table 3.

The same six fog classes were observed during both the ASCOS campaign and based on IGRA profiles over East Greenland. As with ASCOS profiles (Sect. 4.2), most fog in East Greenland occurs with a low-level inversion (Classes 3–6: 66–79% of station soundings,  $p < 0.001$ ). Fog with a surface-based inversion (Class 2) represents only 12–14% of station soundings and does not differ significantly between stations. Excluded soundings (Class 1) are most common at the Ittoqqortoormiit station (21% of soundings,  $\chi^2 = 4.98$ ,  $p = 0.015$ ,  $df = 2$ ), which is related to the  $1^\circ\text{C } T_{\text{dds}}$  threshold (see Fig. 2). Deep fog layers penetrating the inversion base (Class 5) are dominant ( $p < 0.001$ ) over the Danmarkshavn station, where they reach 28% of occurrence, and this was also the dominant class over the Arctic Ocean. There is a non-significant ( $p = 0.054$ ) tendency towards a higher occurrence of this class over the Danmarkshavn station compared to the other stations. For all three stations combined, Class 5 was the most dominant class (23%,  $p = 0.002$ ). Shallow fog-layer occurrence below an inversion base (Class 3) significantly increases with decreasing latitude ( $\chi^2$  range = 6.52–9.85,  $p < 0.001$ ,  $df = 2$ , see Table 3), where Class 3 is also the dominant class (33%,  $p < 0.001$ ). This class was more frequent in East Greenland than during the ASCOS campaign. Class 6 was the least frequent class reported for all stations combined (10%,  $p < 0.001$ ). While all fog with a surface-based inversion (Class 2) was characterized by stably-stratified conditions ( $\mu > 0$ ), fog with a low-level inversion (Classes 3–6) may occur under either stable ( $\mu > 0$ ) or neutral/unstable conditions ( $\mu \leq 0$ ) (Table 2). There is a tendency towards more unstable surface conditions for classes with a low-level inversion (Classes 3–6); however, this was only significant for Class 6 ( $p$  range  $\leq 0.001$ –0.021). Even though there is a tendency for fog at the Ittoqqortoormiit station to occur most often under unstable conditions, this is not statistically significant and it is concluded that all sites present similar characteristics in terms of stability occurrence for each specific class.

Figure 7 displays 120-h (5-day) airmass back-trajectories at 600 m a.g.l. (after Tjernström et al. 2015) for the most common fog types (Table 2) at Tasiilaq (Class 3) and Danmarkshavn stations (Class 5) over the period 2000–2012, with concurrent 850-hPa wind directions for the entire study period (1980–2012). All distributions were tested for their significance using binomial statistical tests at the 95% confidence level. This analysis of back-trajectories and frequency distributions of upper-air wind directions suggests that certain fog classes coincide with distinct airmass origins. Class 5 at the Danmarkshavn station is mostly of oceanic origin (18 out of 27 back-trajectories). The majority of these airmasses originated from lower latitudes, but some originated from the Arctic Ocean. Approximately 60% of soundings

**Table 2** Statistics of fog classes for Danmarkshavn, Itoqortoormiit and Tasilaq stations

	Danmarkshavn				Itoqortoormiit				Tasilaq			
	<i>n</i>	<i>f</i> (%)	<i>F</i> (%)		<i>n</i>	<i>f</i> (%)	<i>F</i> (%)		<i>n</i>	<i>f</i> (%)	<i>F</i> (%)	
Class 1	21		11		25		21		10		9	
Class 2	26		14		17		14		14		12	
Class 3	22		12		25		21		38		33	
$\mu_s \leq 0$	15	68			17	68			24	63		
$\mu_s > 0$	7	32			8	32			14	37		
Class 4	43		23		23		19		19		17	
$\mu_s \leq 0$	26	60			17	74			13	68		
$\mu_s > 0$	17	40			6	26			6	32		
Class 5	52		28		20		17		23		20	
$\mu_s \leq 0$	25	48			14	70			14	61		
$\mu_s > 0$	27	52			6	30			9	39		
Class 6	23		12		11		9		10		9	
$\mu_s \leq 0$	22	96			11	100			9	90		
$\mu_s > 0$	1	4			0	0			1	10		
Total	187		100		121		100		114		100	

Classes 3–6 can have neutral/unstable ( $\mu_s \leq 0$ ) or stable ( $\mu_s > 0$ ) surface layers. Class 2 always has stable surface layers ( $\mu_s > 0$ ). *n* is the number of observations, *f* is the frequency of occurrence of a subclass ( $\mu_s \leq 0$  or  $\mu_s > 0$ ) with respect to the total number of observations for a station's class, and *F* is the frequency of occurrence of a class with respect to the total number of observations for that station

**Table 3** Observed number of occurrence, expected values (italics) and  $\chi^2$  values (in brackets) of fog thermodynamic classes over Danmarkshavn, Ittoqqortoormiit and Tasiilaq stations

	Danmarkshavn	Ittoqqortoormiit	Tasiilaq
Class 1			
21	25	10	
24.82	<i>16.06</i>	<i>15.13</i>	
(0.59)	<b>(4.98)</b>	(1.74)	
Class 2			
26	17	14	
25.26	<i>16.34</i>	<i>15.40</i>	
(0.02)	(0.03)	(0.13)	
Class 3			
22	25	38	
37.67	<i>24.37</i>	<i>22.96</i>	
<b>(6.52)</b>	(0.02)	<b>(9.85)</b>	
Class 4			
43	23	19	
37.67	<i>24.37</i>	<i>22.96</i>	
(0.76)	(0.08)	(0.68)	
Class 5			
52	20	23	
42.10	<i>27.24</i>	<i>25.66</i>	
(2.33)	(1.92)	(0.28)	
Class 6			
23	11	10	
19.50	<i>12.62</i>	<i>11.89</i>	
(0.63)	(0.21)	(0.30)	

Significant  $\chi^2$  values at the 95% confidence level are in bold. The overall  $\chi^2$  and  $p$  values of the contingent table are 31.043 and 0.0006, respectively

of Class 5 (Fig. 7c) and Class 6 (not shown) at the Danmarkshavn station were related to flow from the ice sheet (westerly to northerly wind directions between  $225^\circ$  and  $360^\circ$ ). Nevertheless, this airmass origin is not as prevalent as for Classes 2–4 at the Danmarkshavn station, for which over 80% of airmasses originated from the ice sheet ( $p = 0.028$ ). At the time of the soundings, Classes 5 and 6 are in fact the only classes for which upper-level flow has a predominantly southerly direction (56% frequency with  $p = 0.001$ , and 52% frequency with  $p = 0.011$ , respectively), although there is a large variability of airmass origin as demonstrated by the back-trajectories in Fig. 7a. These combined observations suggest that Classes 5 and 6 are mostly associated with oceanic airmasses.

For Class 3 over the Tasiilaq station, 11 out of 15 back-trajectories originate from the ice sheet and are associated with anticyclonic conditions over Greenland (Fig. 7b). Compared to other classes at the Tasiilaq station, Class 3 has the highest frequency of airmasses originating from the ice sheet (65%;  $p = 0.002$ ). This is in contrast with the Danmarkshavn station, where Class 2 is almost always associated with airmasses originating over the ice sheet (92% frequency of upper winds,  $p < 0.001$ , not shown). When Class 2 is observed, surface conditions are predominantly calm, with backing (counterclockwise change with altitude) or neutral vertical wind profiles, and clear anticyclonic conditions occurring over Greenland according to the back-trajectories and weather charts. Based on these three conditions and

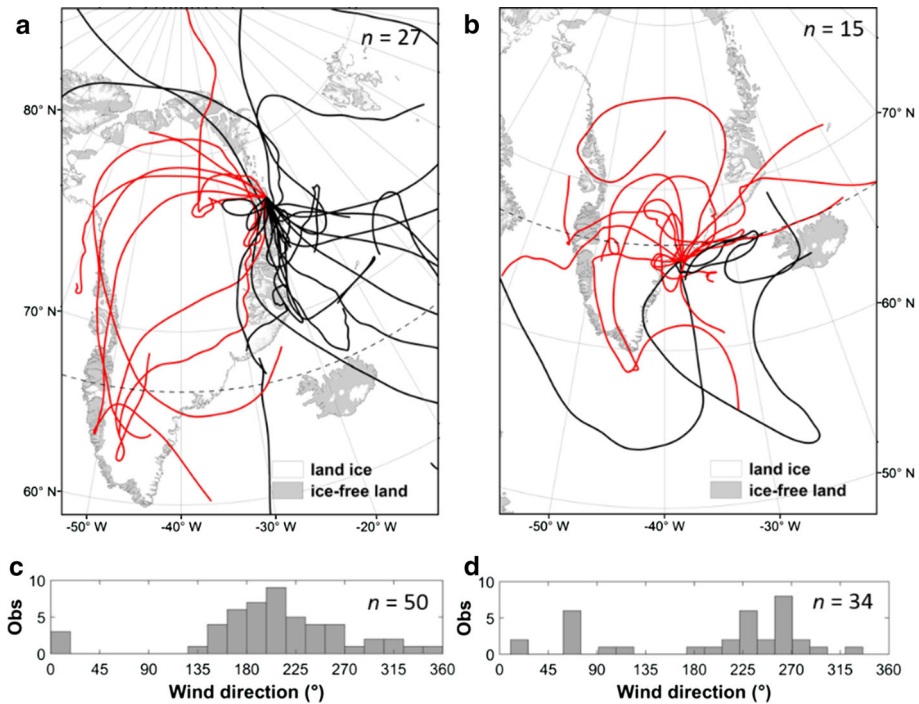


**Fig. 7** All 600-m a.g.l. 120-h back-trajectories of air masses in 2000–2012 associated with **a** Class 5 over the Danmarkshavn station, and **b** Class 3 over the Tasiilaq station. Black lines are predominantly oceanic air masses and red lines have travelled over the Greenland ice sheet. Lower panels are the frequency distributions of wind directions at the 850-hPa radiosonde level for the entire period 1980–2012 for **c** Class 5 over the Danmarkshavn station, and **d** Class 3 over the Tasiilaq station. Numbers of observations ( $n$ ) are displayed in the upper right corner of each panel. Back-trajectories are from the NOAA HYSPLIT model (<http://www.ready.noaa.gov>)

the Class 2 thermodynamic profiles, we infer that some Class 2 fog cases may be radiation fog (e.g. Roach et al. 1976; Croft et al. 1997).

#### 4.4 Support for IGRA Fog-Process Interpretation from Time-Lapse Images

One month of time-lapse observations (1452 30-min interval images) collected during July–August 2011 were analyzed visually to understand fog processes at the mouth of Sermilik Fjord near the Tasiilaq station. Of 151 images with fog, 16 could be classified as being of the advective type and nine occurred through stratus-base lowering (Fig. 8a, b). Fog often displayed a sharp top, which is typical of thermally and dynamically stable atmospheric conditions (e.g. Koračin 2017). Dissipation processes included fog retreat towards the ocean (12 images), fog lifting to a stratus (eight images, Fig. 8d), or dissipation from top by radiative heating or mixing processes (five images) (cf. Gulpepe et al. 2016). Multiple low-level cloud layers were observed during both formation (five images) and dissipation stages (six images, Fig. 8c, d). Stratus-base lowering and fog lifting processes were found to occur within a period of 1.5–3 h.



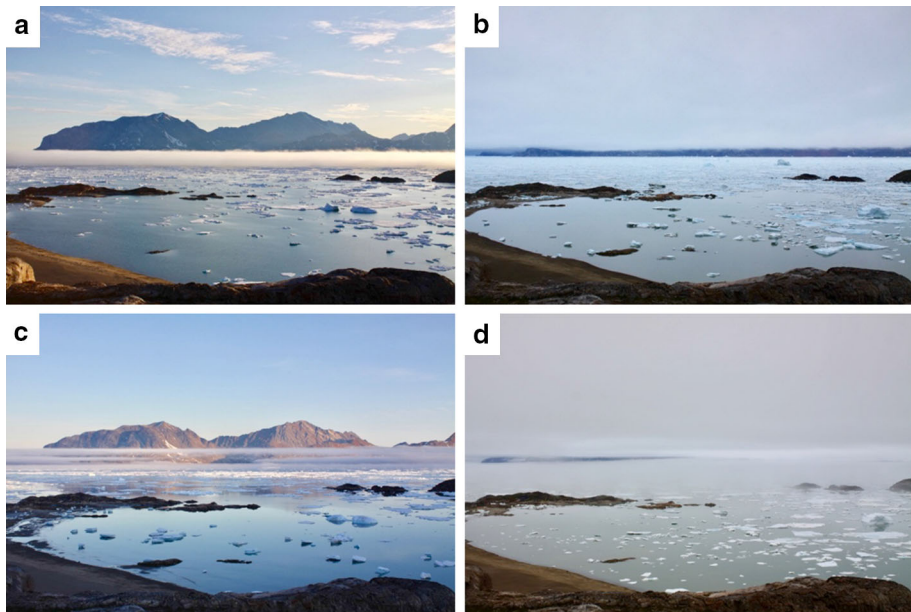


**Fig. 8** Examples of fog observations obtained from the time-lapse camera located at the mouth of Sermilik Fjord: **a** advection fog entering the fjord, **b** stratus-base lowering into fog, **c** dissipating fog with several layers of low stratus, and **d** fog separating from stratus via subsaturation between the two layers (dissipation). The camera is approximately facing south-west, the open ocean is to the left and the inner fjord to the right

## 5 Discussion

### 5.1 Comparison with Arctic Stratocumulus Clouds

Studies of sea-fog thermodynamic structure have mostly been restricted to mid-latitudes (e.g. Pilié et al. 1979; Zhang et al. 2009; Huang et al. 2015) and the thermodynamic structure of Arctic summer fog using in-situ radiosonde observations has previously not been published. The only available field measurements of Arctic fog-top with respect to inversion-base height are from Sotiropoulou et al. (2016). We, therefore, mainly discuss our results in relation to studies of Arctic stratocumulus clouds. This is justified because, (i) both are marine stratiform boundary-layer clouds usually capped by an inversion (Cotton and Anthes 1989; Gultepe 2007; Wood 2012); (ii) both frequently originate from warm-air advection (Nilsson and Bigg 1996; Sedlar et al. 2012; Shupe et al. 2013; Sotiropoulou et al. 2014, 2016; Huang et al. 2015; Tjernström et al. 2015); (iii) fog has geometrical characteristics similar to stratocumulus clouds (Welch and Wielicki 1986); (iv) transitions can occur between these cloud types (Koračin et al. 2001, 2014; Gao et al. 2007; Huang et al. 2015); and (v) stratocumulus clouds are the predominant cloud type in the Arctic melt season (Eastman and Warren 2010) and studies over the Arctic Ocean have, therefore, mainly focused on the thermodynamic structure of these clouds (Sedlar and Tjernström 2009; Sedlar et al. 2012; Sotiropoulou et al. 2014).

Similarities between our findings and other studies of Arctic fog or stratocumulus clouds over Arctic pack ice during the melt season lead us to four main conclusions: (i) the majority of fog/stratocumulus events occur with a low-level inversion (cf. Sedlar and Tjernström 2009; Sedlar et al. 2012); (ii) vertically-extensive fog or stratocumulus penetrating the inversion

layer are the most common type at high-Arctic locations. These can be related to the poleward advection of heat and moisture over cold surfaces (cf. Sedlar and Tjernström 2009; Sedlar et al. 2012; Shupe et al. 2013) and are facilitated by a higher year-round sea-ice concentration at these northern locations (Sotiropoulou et al. 2016); (iii) fog/stratocumulus below, or capped by, an inversion layer is more frequent at locations closest to the coast and at lower latitudes, where sea-ice concentrations are lower (cf. Sedlar et al. 2012; Sotiropoulou et al. 2016); and (iv) surface layers are frequently statically neutral or unstable during fog/stratocumulus cloud conditions (cf. Sedlar et al. 2012; Shupe et al. 2013; Sotiropoulou et al. 2014).

## 5.2 Arctic Fog Formation and Dissipation Process Interpretation

The integrated analysis of time-lapse images, airmass back-trajectories, ASCOS microwave radiometer temperature retrievals and fog-process literature, suggests that fog thermodynamic classes in coastal East Greenland represent stages of development of advection fog, stratus-base lowering, or fog lifting. We infer two main mechanisms of fog formation and three mechanisms of fog dissipation, and illustrate these in Fig. 9 by specific transitions between thermodynamic profiles. Figure 9a displays a typical development of advection fog from a warm and moist airmass cooled down to its dew-point temperature by contact with sea-ice or cold water (e.g. Fig. 8a) transported inland by a sea breeze (Alt 1979; Cappelen 2015). As this fog grows, radiative cooling at its top results in a transition from a surface-based to a low-level inversion (cf. Sotiropoulou et al. 2014; Kim and Yum 2017). Figure 9b illustrates fog formation by stratus-base lowering (e.g. Fig. 8b). The turbulence generated by cloud-top radiative cooling, combined with the evaporation of cloud droplets below the cloud base, results in an increase in humidity and the downward migration of the cloud base (Cotton and Anthes 1989). In Fig. 9c, d, dissipation of fog due to drying and/or warming at the fog-top results in thinning of the fog layer. This reduction in relative humidity may be caused by entrainment of warm, dry air from aloft into the fog layer or by solar heating at the fog-top (Gultepe et al. 2016). Both processes result in a drier profile in the mixed layer (i.e. Classes 3 and 4). This profile transition from Class 5 to 4 to 3 is also observed when fog retreats towards the ocean (Fig. 9c). In Fig. 9e, large subsidence warming strengthens the inversion, lowers its base, and eventually switches the thermodynamic profile from a low-level to a surface-based inversion. This results either in thinning of a fog layer and a transition from Class 5 to Class 2 (Koračin et al. 2001; Lewis et al. 2003; Fig. 9e), or in fog formation when the initial stage is a stratus cloud (Class 1 instead of Class 5 on Fig. 9e, not shown). Altogether, Fig. 9c–e represent fog dissipation by heating and mixing. In contrast, Fig. 9f depicts the dissipation mechanism of fog lifting to a stratus. Here, Class 6 is a transition profile between the stages of a mature fog (Class 5) and a stratus cloud (Class 1). Class 6 almost exclusively occurs under statically unstable surface conditions over East Greenland, which is consistent with increased turbulence at the surface that leads to a fog-lifting mechanism (Cotton and Anthes 1989; Koračin et al. 2001).

Since Class 3 is the dominant fog class over the Tasiilaq station only, we infer that fog dissipation processes presented in Fig. 9c, d occur more frequently in south-east Greenland. This enhanced dissipation is consistent with the shorter fog duration at the Tasiilaq station compared to that at the Danmarkshavn and Ittoqqortoormiit stations (Gueye 2014). Sedlar et al. (2012) found that stratocumulus clouds capped by or occurring below an inversion base were more frequent over Barrow, coastal northern Alaska, than over the Arctic Ocean. Our results also show that fog Classes 3 and 4 are more frequent over East Greenland than in the high-Arctic Ocean ASCOS data. The majority of back-trajectories for Class 3 over the Tasiilaq station (Fig. 7b) are associated with drier and colder airmasses originating from

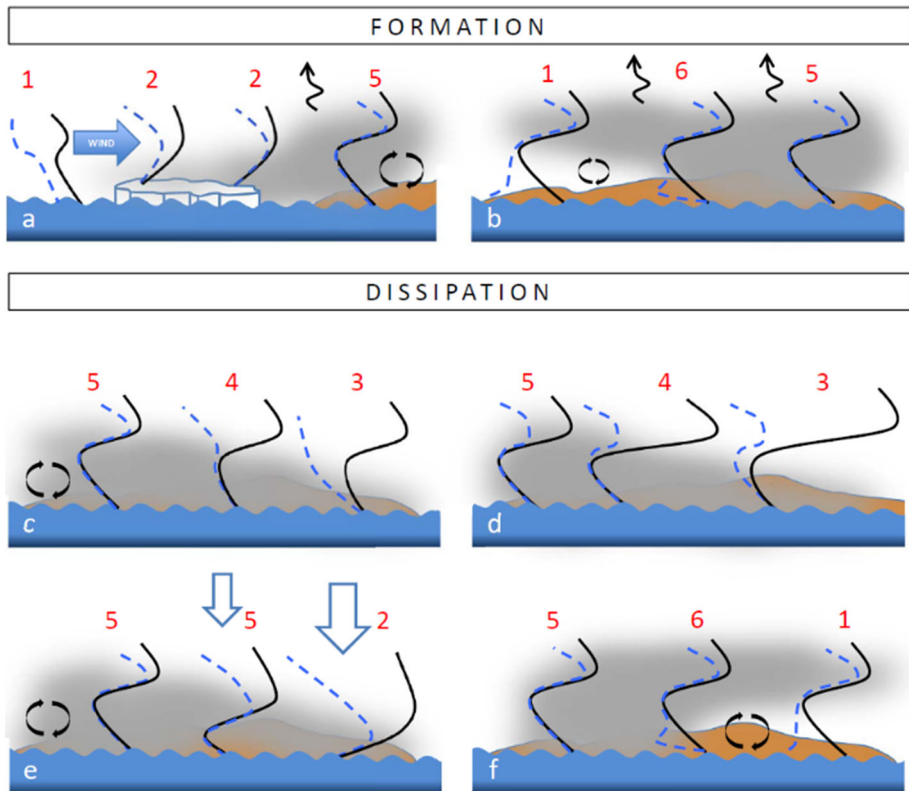


**Fig. 9** Fog formation **a, b** and dissipation **c–f** mechanisms based on thermodynamic profiles: **a** advection fog development and growth, **b** stratus-base lowering into fog, **c** fog thinning and dissipation through drying out due to entrainment of drier air from aloft, **d** fog thinning and dissipation due to warming aloft driven by entrainment of warm air and/or solar heating, **e** fog thinning and dissipation through large-scale subsidence (vertical arrows), and **f** fog lifting to stratus. Fog classes are shown in red. Black curves are temperature profiles and dashed blue curves are dew-point temperature profiles

the ice sheet. This airmass origin, in combination with the fjord topography of south-east Greenland, likely promote fog dissipation through strong seaward katabatic flow (Klein and Heinemann 2002; Cappelen 2015). Another factor that could lead to increased fog dissipation is the latitudinal effect: the Tasiilaq station has stronger diurnal variations of the solar elevation angle and lower sea-ice concentrations in summer, leading to less fog formation and shorter fog duration at the Tasiilaq station than at the Danmarkshavn station (Gueye 2014). Lastly, land surface heating and turbulence can enhance fog dissipation in coastal environments (Serreze and Barry 2014; Cappelen 2015), in part by generating stronger land-breeze and sea-breeze cycles. The coastward advection and seaward retreat of fog associated with these breezes (Cappelen et al. 2001) result in a stronger diurnal fog cycle at the lower-latitude coastal stations than at the higher-latitude stations and over Arctic pack ice (Uttal et al. 2002; Tjernström et al. 2014). In summary, we hypothesize that Classes 3 and 4 at the Tasiilaq station represent dissipating stages of fog driven by a combination of the more pronounced solar diurnal cycle and land- and sea-breeze cycles, and the more frequent katabatic flow enhancing turbulence at this station. It cannot be determined from our analysis which of these environmental factors is dominant in causing fog dissipation, and the concepts need to

be further examined using numerical fog models (e.g. Gao et al. 2007; Bergot 2016; Koračin 2017).

### 5.3 Data Uncertainties and Dew-Point Depression Threshold Sensitivity

Uncertainties linked to data collection, analyses and instrumental errors may limit the value of process-related observations and understanding. In addition to IGRA sounding sensor accuracy and pre-processing uncertainties that include the surface-level sounding being a mixture of radiosonde data and adjacent weather station data, the major uncertainty in our method is in assigning an optimal surface dew-point depression ( $T_{\text{dds}}$ ) threshold. In order to quantify this uncertainty, a sensitivity analysis was performed to explore whether the dominant classes under the  $T_{\text{dds}} = 1^\circ\text{C}$  threshold remain the same under a range of  $T_{\text{dds}}$  thresholds ( $T_{\text{dds}} = 0$  to  $2^\circ\text{C}$ , based on  $1^\circ \pm 1^\circ\text{C}$  to account for instrument uncertainties corresponding to  $RH_w = 85\text{--}100\%$ ). For all  $T_{\text{dds}}$  thresholds, we constrained the sum of soundings in all fog classes together for each station to the sum of fog soundings that were captured by the original  $T_{\text{dds}} = 1^\circ\text{C}$  threshold at each respective station (see Table 1). We applied this restriction in order to better assess the proportional changes between fog classes at each station. The frequency distribution for each fog class under each threshold is reported in Fig. 10. Optimal  $T_{\text{dds}}$  thresholds were calculated based on the frequency distribution of Class 1, by maximizing the distance between the Class 1 curve and the straight line connecting  $T_{\text{dds}} = 0$  and  $2^\circ\text{C}$  (Fig. 10 upper left panel). The calculated optimal thresholds are  $0.7^\circ\text{C}$  for the Danmarkshavn and Ittoqqortoormiit stations and  $0.4^\circ\text{C}$  for the Tasiilaq station. These optimal thresholds remained unchanged when selecting a smaller domain (e.g. from 0 to  $1.5^\circ\text{C}$ ). Different optimization techniques could have resulted in marginal differences between optimal thresholds, but the shapes of the Class 1 curves in Fig. 10 demonstrate that the optimal threshold is always below  $1^\circ\text{C}$ . Relative frequency of fog Classes 3–6, fog with a low-level inversion, is most affected by modifying the optimal threshold relative to  $T_{\text{dds}} = 1^\circ\text{C}$  (Fig. 10). Yet, Classes 3 and 5 remain dominant for all thresholds. The consistent choice of a  $T_{\text{dds}} = 1^\circ\text{C}$  threshold instead of an optimal threshold unique to each station, therefore, neither affects our overall interpretation of fog classes as related to the spatial distribution of fog processes, nor does this choice affect our inferred transitions between classes.

The automated fog classification method presented herein requires the use of synoptic weather observations at stations collocated with the radiosonde launch site. When the  $T_{\text{dds}} = 1^\circ\text{C}$  threshold was applied to all IGRA summer soundings at the three East Greenland stations, irrespective of weather type, more apparent fog cases were returned than the 25–36% actual fog occurrence reported from the synoptic weather codes. These false positives included precipitation (31–48%), mist (14–20%) and no significant weather reported (7–13%). The last category is the only unexplained false positive, since small  $T_{\text{dds}}$  values in the precipitation and mist categories can result from evaporation of the precipitation.

Radiosonde profiles that are not simultaneous with surface observations will likely result in more Class 1 assignment of fog, particularly when fog is discontinuous in space or time. To investigate this, we compared the frequency of fog thermodynamic Class 1 for soundings simultaneous with synoptic observations to the frequency of Class 1 in all soundings. Although its proportion remained unchanged for the Ittoqqortoormiit station (25% exclusions), soundings simultaneous with synoptic fog observations only have 2% of excluded events at the Danmarkshavn station and no exclusions at the Tasiilaq station.

Due to increased vertical resolution through time, radiosonde instrument changes and sounding station relocations, IGRA soundings are suggested to be poorly-suited for longi-

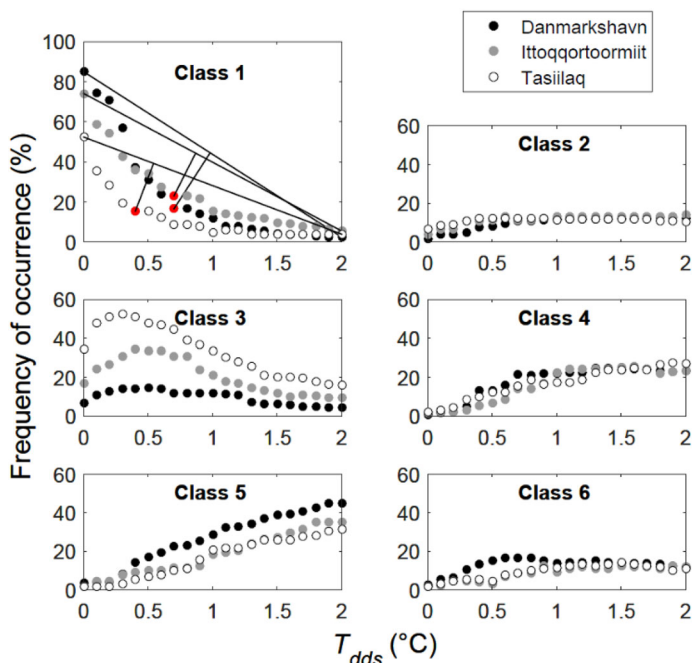


**Fig. 10** Frequency of fog classes as a function of surface dew-point depression threshold ( $T_{dds}$ ). Red dots are optimal  $T_{dds}$  determined from the maximum orthogonal distance (lines perpendicular to straight line joining first and last point) of Class 1 distribution. Note that the vertical scale for Class 1 is different, as the lowest values in the range of  $T_{dds}$  lead to a high frequency of exclusions

tudinal studies (Durre and Yin 2008; Zhang and Seidel 2011). However, these three main data inhomogeneities are negligible for post-1992 Greenland IGRA data (Box and Cohen 2006). Applying our fog classification to the post-1992 period only does not change the relative proportion of fog classes at Tasiilaq and Ittoqqortoormiit stations, while at the Danmarkshavn station it results in fewer excluded events (Class 1). Thus, despite possible data inhomogeneities in the 1980–1992 period, our fog classification method is found to be robust and its results are valid for the entire 1980–2012 period analyzed.

The IGRA dataset is considered appropriate for studying the structure of the boundary layer (e.g. Zhang et al. 2011) and Ingleby et al. (2014) determined that significant levels from IGRA soundings accurately reproduce the original high-resolution soundings. However, we question the ability of IGRA's significant levels to capture small-scale structures such as multi-layer low-level clouds. These features are frequently observed in our time-lapse imagery, but were never detected in any of the East Greenland IGRA data. Yet, we frequently observed multi-layer low-level clouds in the higher-resolution ASCOS radiosonde profiles.

## 6 Summary and Conclusions

This study presented a novel automated method for classifying Arctic fog using thermodynamic profiles taken from the Integrated Global Radiosonde Archive (IGRA) database and World Meteorological Organization (WMO) present-weather observations. Observations

from the period 1980–2012 at three stations in coastal East Greenland were classified into six distinct fog classes using the following conditions to separate thermodynamic profiles: a 1 °C surface dew-point depression threshold, static stability of the surface layer, lower tropospheric inversion type, and fog-top height with respect to the inversion-base height. Despite differences in vertical resolution and environmental conditions of ASCOS (Arctic Ocean) and IGRA (coastal East Greenland) radiosonde observations, the same fog classes were inferred. Using these six fog classes together with airmass back-trajectories, time-lapse images, and ASCOS microwave radiometer temperature retrievals, we hypothesize that these classes represent different stages of advection fog formation, development, and dissipation, including stratus-base lowering and fog lifting.

The thermodynamic structure of fog occurring during the Arctic melt season was characterized and found to be consistent with earlier work on Arctic fog (Sotiropoulou et al. 2016) and on Arctic stratocumulus clouds (Sedlar and Tjernström 2009; Sedlar et al. 2012; Shupe et al. 2013; Sotiropoulou et al. 2014). Both boundary-layer cloud types usually occur under unstable surface-layer conditions and with an elevated inversion base. At high latitudes, fog and stratocumulus clouds frequently penetrate the inversion base. The analysis of airmass back-trajectories supports the poleward advection of heat and moisture hypothesized by Sedlar et al. (2012) to explain the persistence of such vertically-extensive fog and low-level clouds at high latitudes, while melting sea-ice may be an additional local factor promoting this thermodynamic characteristic (Sotiropoulou et al. 2016). At lower latitudes, fog and stratocumulus below or capped by the inversion layer are more frequent. This is likely caused by enhanced dissipation processes, resulting from a higher solar elevation angle, a higher or more complex topography and airmasses originating from the ice sheet and adjacent land. Additionally, fog and stratocumulus below or capped by the inversion could be due to a more local or regional fog-formation process, which is in contrast to the long-range advection of moisture (e.g. Sedlar et al. 2012).

The thermodynamic classification described here can be applied to any polar weather station and allows investigation of predominantly liquid-phase fog processes and microphysical properties at high latitudes. In future studies, our results could be used in combination with data from cloud satellites, vessel-based and ground-based projects (e.g. Gultepe et al. 2014) to extend fog research in polar regions. Outcomes from such multi-faceted research may lead to improvement in detection, monitoring and prediction of Arctic fog, as well as to a better understanding of fog and low-cloud microphysical and dynamical processes, which play an important role in the Arctic surface energy budget.

**Acknowledgements** This work was supported by the Natural Sciences and Engineering Research Council of Canada (to HJ), Alberta Innovates Technology Futures (to GFG) and University of Lethbridge funding. Time-lapse imagery was collected by TDJ with support from INTERACT under the European Community's Seventh Framework Programme. The authors gratefully acknowledge the Danish Meteorological Institute (DMI) for the distribution of East Greenland synoptic weather data, the Arctic Summer Cloud Ocean Study (ASCOS) for the provision of their data, the National Oceanic and Atmospheric Administration (NOAA) for access to the Integrated Global Radiosonde Archive dataset, and the NOAA Air Resources Laboratory for their release of the HYSPLIT transport and dispersion model data. The Matlab script to extract IGRA data was provided by Dr. Andy Rhines (University of Washington). Discussions with Dr. Jakob Abermann (Asiaq, Greenland Survey) directed part of this work towards the use of microwave radiometer retrievals. Drs. Matt Letts, Chris Hopkinson, Phil Bonnaventure and Rob Laird (University of Lethbridge) are acknowledged for their encouragement and critical feedback. Finally, the authors would like to particularly thank two anonymous reviewers for their valuable feedback.



## References

- Alt BT (1979) Investigation of summer synoptic climate controls on the mass balance of Meighen Ice Cap. *Atmos Ocean* 17(3):181–199
- American Meteorological Society (2015) Sea fog. Glossary of Meteorology. [http://glossary.ametsoc.org/wiki/Sea\\_fog](http://glossary.ametsoc.org/wiki/Sea_fog). Accessed 1 Feb 2018
- Antikainen V, Paukkunen A, Jauhiainen H (2002) Measurement accuracy and repeatability of Vaisala RS90 Radiosonde. *Vaisala News* 159:11–13
- Bendix J (1995) A case study on the determination of fog optical depth and liquid water path using AVHRR data and relations to fog liquid water content and horizontal visibility. *Remote Sens* 16(3):515–530
- Bennartz R, Shupe MD, Turner DD, Walden VP, Steffen K, Cox CJ, Hulie MS, Miller NB, Pettersen C (2013) July 2012 Greenland melt extent enhanced by low-level liquid clouds. *Nature* 496(7443):83–86
- Bergot T (2016) Large-eddy simulation study of the dissipation of radiation fog. *Q J R Meteorol Soc* 142:1029–1040
- Bødtker E (2003) Observation systems 2003, technical report 03-16, Ministry of Transport, Danish Meteorological Institute, Copenhagen
- Box JE, Cohen AE (2006) Upper-air temperatures around Greenland: 1964–2005. *Geophys Res Lett.* <https://doi.org/10.1029/2006GL025723>
- Braun C, Hardy DR, Bradley RS, Sahanatian V (2004) Surface mass balance of the Ward Hunt Ice Rise and Ward Hunt Ice Shelf, Ellesmere Island, Nunavut, Canada. *J Geophys Res Atmos* 109(D22):1–9
- Cappelen J (2015) Greenland—DMI historical climate data collection 1784–2014. Technical report 15-04, Danish Meteorological Institute, Copenhagen
- Cappelen J, Jørgensen BV, Laursen EV (2001) The observed climate of Greenland, 1958–99—with climatological standard normals, 1961–90. Technical report 00-18, Danish Meteorological Institute, Copenhagen
- Chutko KJ, Lamoureux SF (2009) The influence of low-level thermal inversions on estimated melt-season characteristics in the central Canadian Arctic. *Int J Climatol* 29(2):259–268
- Circumpolar Arctic Vegetation Map (CAVM) (2003) Scale: 1:7,500,000. Conservation of Arctic flora and fauna (CAFF) Map No. 1. U.S. Fish and Wildlife Service, Anchorage, Alaska
- Cotton WR, Anthes RA (1989) Fogs and Stratocumulus Clouds. In: Cotton WR, Anthes RA (eds) *Storm and cloud dynamics*. International geophysics series 44. Academic Press, San Diego, pp 303–367
- Croft PJ, Post RL, Medlin JM, Johnson GA (1997) Fog forecasting for the southern region: a conceptual model approach. *Weather Forecast* 12(3):545–556
- Curry JA, Ebert EE, Herman GF (1988) Mean and turbulence structure of the summertime Arctic cloudy boundary layer. *Q J R Meteorol Soc* 114(481):715–746
- Curry JA, Schramm JL, Rossow WB, Randall D (1996) Overview of Arctic cloud and radiation characteristics. *J Clim* 9(8):1731–1764
- Deser C, Tomas R, Alexander M, Lawrence D (2010) The seasonal atmospheric response to projected Arctic sea ice loss in the late 21st century. *J Clim* 23(2):333–351
- Devasthale A, Willén U, Karlsson K-G, Jones CG (2010) Quantifying the clear-sky temperature inversion frequency and strength over the Arctic Ocean during summer and winter seasons from AIRS profiles. *Atmos Chem Phys* 10(12):5565–5572
- Durre I, Yin X (2008) Enhanced radiosonde data for studies of vertical structure. *Bull Am Meteorol Soc* 89(9):1257–1262
- Durre I, Vose RS, Wuertz DB (2006) Overview of the Integrated Global Radiosonde Archive. *J Clim* 19(1):53–68
- Eastman R, Warren SG (2010) Arctic cloud changes from surface and satellite observations. *J Clim* 23(15):4233–4242
- Gaffen DJ (1993) Historical changes in radiosonde instruments and practices. WMO/TD-No. 541. Instruments and observing methods report no. 50. World Meteorological Organization, Geneva, Switzerland
- Gao S, Lin H, Shen B, Fu G (2007) A heavy sea fog event over the Yellow Sea in March 2005: analysis and numerical modeling. *Adv Atmos Sci* 24(1):65–81
- Gardner AS, Sharp M (2007) Influence of the arctic circumpolar vortex on the mass balance of Canadian High Arctic glaciers. *J Clim* 20(18):4586–4598
- Gueye S (2014) Frequency, timing and temporal patterns of regional coastal Arctic fog in East Greenland. MSc Research Thesis, University of Amsterdam (Netherlands)
- Gultepe I (2007) *Fog and boundary layer clouds: fog visibility and forecasting*. Springer Science and Business Media, Basel
- Gultepe I, Tardif R, Michaelides SC, Cermak J, Bott A, Bendix J, Müller MD, Pagowski M, Hansen B, Ellrod E, Jacobs W, Toth G, Cober SG (2007) Fog research: a review of past achievements and future perspectives. *Pure Appl Geophys* 164(6–7):1121–1159



- Gultepe I, Kuhn T, Pavolonis M, Calvert C, Gurka J, Heymsfield AJ, Liu PSK, Zhou B, Ware R, Ferrier B, Milbrandt J, Bernstein B (2014) Ice fog in arctic during FRAM–Ice Fog project: aviation and nowcasting applications. *Bull Am Meteorol Soc* 95(2):211–226
- Gultepe I, Fernando HJS, Pardyjak ER, Hoch SW, Silver Z, Creegan E, Leo LS, Pu Z, De Wekker FJ, Hang C (2016) An overview of the MATERHORN fog project: observations and predictability. *Pure appl Geophys* 173(9):2983–3010
- Hanesiak JM, Wang XL (2005) Adverse-weather trends in the Canadian Arctic. *J Clim* 18(16):3140–3156
- Hanna E, Cappelen J (2003) Recent cooling in coastal southern Greenland and relation with the North Atlantic Oscillation. *Geophys Res Lett*. <https://doi.org/10.1029/2002GL015797>
- Hardy B (1998) Determination of relative humidity in subzero temperatures. Technical Report RH\_WMO, RH System, Albuquerque, New Mexico
- Heintzenberg J, Leck C, Birmili W, Wehner B, Tjernström M, Wiedensohler A (2006) Aerosol number–size distributions during clear and fog periods in the summer high Arctic: 1991, 1996 and 2001. *Tellus B* 58(1):41–50
- Huang H, Liu H, Huang J, Mao W, Bi X (2015) Atmospheric boundary layer structure and turbulence during sea fog on the southern China coast. *Mon Weather Rev* 143(5):1907–1923
- Hulth J, Rolstad C, Trondsen K, Rodby RW (2010) Surface mass and energy balance of Sorbreen, Jan Mayen, 2008. *Ann Glaciol* 51(55):110–119
- Ingleby B, Fucile E, Vasiljevic D, Kral T, Isaksen I (2014) Use of BUFR radiosonde and surface observations at ECMWF. In: Using ECMWF forecast workshop, 4–6 June 2014, Reading, UK
- IPCC (2013) Summary for policymakers. In: Stocker TF, Qin D, Plattner G-K, Tignor M, Allen SK, Boschung J, Nauels A, Xia Y, Bex V, Midgley PM (eds) *Climate change 2013: the physical science basis. Contribution of working group I to the fifth assessment report of the intergovernmental panel on climate change*. Cambridge University Press, Cambridge, pp 1–30
- Kahl JD (1990) Characteristics of the low-level temperature inversion along the Alaskan Arctic coast. *Int J Climatol* 10(5):537–548
- Kahl JD, Serreze MC, Schnell RC (1992) Tropospheric low-level temperature inversions in the Canadian Arctic. *Atmos Ocean* 30(4):511–529
- Kim CK, Yum SS (2010) Local meteorological and synoptic characteristics of fogs formed over Incheon international airport in the west coast of Korea. *Adv Atmos Sci* 27(4):761–776
- Kim CK, Yum SS (2017) Turbulence in marine fog. In: Koraćin D, Dorman CE (eds) *Marine fog: challenges and advancements in observations, modeling, and forecasting*. Springer International Publishing, Berlin, pp 245–271
- Klein T, Heinemann G (2002) Interaction of katabatic winds and mesocyclones near the eastern coast of Greenland. *Meteorol Appl* 9(4):407–422
- Koerner RM (2005) Mass balance of glaciers in the Queen Elizabeth Islands, Nunavut, Canada. *Ann Glaciol* 42(1):417–423
- Koraćin D (2017) Modeling and forecasting marine fog. In: Koraćin D, Dorman C (eds) *Marine fog: challenges and advancements in observations, modeling, and forecasting*. Springer International Publishing, Cham, pp 425–475
- Koraćin D, Lewis J, Thompson WT, Dorman CE, Businger JA (2001) Transition of stratus into fog along the California coast: observations and modeling. *J Atmos Sci* 58(13):1714–1731
- Koraćin D, Dorman CE, Lewis JM, Hudson JG, Wilcox EM, Torregrosa A (2014) Marine fog: a review. *Atmos Res* 143:142–175
- Leipper DF (1994) Fog on the US west coast: a review. *Bull Am Meteorol Soc* 75(2):229–240
- Lewis SM, Smith LC (2009) Hydrologic drainage of the Greenland ice sheet. *Hydrol Process* 23(14):2004–2011
- Lewis JM, Koraćin D, Rabin R, Businger J (2003) Sea fog off the California coast: viewed in the context of transient weather systems. *J Geophys Res Atmos*. <https://doi.org/10.1029/2002JD002833>
- Liu Y, Key JR, Liu Z, Wang X, Vavrus SJ (2012) A cloudier Arctic expected with diminishing sea ice. *Geophys Res Lett*. <https://doi.org/10.1029/2012GL051251>
- Mernild SH, Hansen BU, Jakobsen BH, Hasholt B (2008) Climatic conditions at the Mittivakkat Glacier catchment (1994–2006), Ammassalik Island, SE Greenland, and in a 109-year perspective (1898–2006). *Geogr Tidsskr Dan J Geogr* 108(1):51–72
- Meyer WD, Rao GV (1999) Radiation fog prediction using a simple numerical model. *Pure Appl Geophys* 155(1):57–80
- Nakanishi M, Niino H (2006) An improved Mellor–Yamada level-3 model: its numerical stability and application to a regional prediction of advection fog. *Boundary Layer Meteorol* 119(2):397–407
- Nardino M, Georgiadis T (2003) Cloud type and cloud cover effects on the surface radiative balance at several polar sites. *Theor Appl Climatol* 74(3–4):203–215

- National Oceanic and Atmospheric Administration (NOAA) (1995) Surface weather observations and reports, Federal Meteorological Handbook No. 1, Department of Commerce, NOAA
- Nilsson ED (1996) Planetary boundary layer structure and air mass transport during the International Arctic Ocean Expedition 1991. *Tellus B* 48(2):178–196
- Nilsson ED, Bigg EK (1996) Influences on formation and dissipation of high arctic fogs during summer and autumn and their interaction with aerosol. *Tellus Ser B Chem Phys Meteorol* 48(2):234–253
- Oke TR (1987) Boundary layer climates, 2nd edn. Methuen & Co. Ltd, London
- Palm SP, Strey ST, Spinhrne J, Markus T (2010) Influence of Arctic sea ice extent on polar cloud fraction and vertical structure and implications for regional climate. *J Geophys Res Atmos*. <https://doi.org/10.1029/2010JD013900>
- Pettersen S (1956) Weather analysis and forecasting, vol 2, 2nd edn. McGraw-Hill Publ. Inc., New York
- Pfeffer WT, Arendt AA, Bliss A, Bolch T, Cogley JG, Gardner AS, Hagen JO, Hock R, Kaser G, Kienholz C, Miles ES, Moholdt G, Mölg N, Paul F, Radić V, Rastner P, Raup BH, Rich J, Sharp MJ, The Randolph Consortium (2014) The Randolph Glacier Inventory: a globally complete inventory of glaciers. *J Glaciol* 60(221):537–552
- Pilić RJ, Mack EJ, Rogers CW, Katz U, Kocmond WC (1979) The formation of marine fog and the development of fog-stratus systems along the California coast. *J Appl Meteorol* 18(10):1275–1286
- Roach WT, Brown R, Caughey SJ, Garland JA, Readings CJ (1976) The physics of radiation fog: I—a field study. *Q J R Meteorol Soc* 102(432):313–333
- Roach WT, Brown R, Caughey SJ, Crease BA, Slingo A (1982) A field study of nocturnal stratocumulus: I. Mean structure and budgets. *Q J R Meteorol Soc* 108(455):103–123
- Sedlar J, Tjernström M (2009) Stratiform cloud-inversion characterization during the Arctic melt season. *Boundary Layer Meteorol* 132(3):455–474
- Sedlar J, Shupe MD, Tjernström M (2012) On the relationship between thermodynamic structure and cloud top, and its climate significance in the Arctic. *J Clim* 25(7):2374–2393
- Serreze MC, Barry RG (2011) Processes and impacts of Arctic amplification: a research synthesis. *Glob Planet Change* 77(1–2):85–96
- Serreze MC, Barry RG (2014) The Arctic climate system. 2nd edition. Cambridge University Press
- Serreze MC, Barrett AP, Slater AG, Steele M, Zhang J, Trenberth KE (2007) The large-scale energy budget of the Arctic. *J Geophys Res Atmos*. <https://doi.org/10.1029/2006JD008230>
- Shupe MD, Intrieri JM (2004) Cloud radiative forcing of the Arctic surface: the influence of cloud properties, surface albedo, and solar zenith angle. *J Clim* 17(3):616–628
- Shupe MD, Persson POG, Brooks IM, Tjernström M, Sedlar J, Mauritsen T, Sjogren S, Leck C (2013) Cloud and boundary layer interactions over the Arctic sea ice in late summer. *Atmos Chem Phys* 13:9379–9400
- Sotiropoulou G, Sedlar J, Tjernström M, Shupe MD, Brooks IM, Persson POG (2014) The thermodynamic structure of summer Arctic stratocumulus and the dynamic coupling to the surface. *Atmos Chem Phys* 14(22):12573–12592
- Sotiropoulou G, Tjernström M, Sedlar J, Achtert P, Brooks BJ, Brooks IM, Persson POG, Prytherch J, Salisbury DJ, Shupe MD, Johnston PE, Wolfe D (2016) Atmospheric conditions during the Arctic clouds in summer experiment (ACSE): contrasting open water and sea ice surfaces during melt and freeze-up seasons. *J Clim* 29(24):8721–8744
- Stein AF, Draxler RR, Rolph GD, Stunder BJB, Cohen MD, Ngan F (2015) NOAA's HYSPLIT atmospheric transport and dispersion modeling system. *Bull Am Meteorol Soc* 96(12):2059–2077
- Steinbrecht W, Claude H, Schönenborn F, Leiterer U, Dier H, Lanzinger E (2008) Pressure and temperature differences between Vaisala RS80 and RS92 radiosonde systems. *J Atmos Ocean Technol* 25(6):909–927
- Stull RB (1988) An introduction to boundary layer meteorology. Kluwer Academic Publishers, Dordrecht
- Svendsen H, Beszczynska-Møller A, Hagen JO, Lefauconnier B, Tverberg V, Gerland S, Ørbæk JB, Bischof K, Papucci C, Zajackowski M, Azzolini R, Bruland O, Wiencke C, Winther J-G, Dallman W (2002) The physical environment of Kongsfjorden-Krossfjorden, an Arctic fjord system in Svalbard. *Polar Res* 21(1):133–166
- Telford JW, Chai SK (1984) Inversions, and fog, stratus and cumulus formation in warm air over cooler water. *Boundary Layer Meteorol* 29(2):109–137
- Tjernström M, Birch CE, Brooks IM, Shupe MD, Persson POG, Sedlar J, Mauritsen T, Leck C, Paatero J, Szczodrak M, Wheeler CR (2012) Meteorological conditions in the central Arctic summer during the Arctic Summer Cloud Ocean Study (ASCOS). *Atmos Chem Phys* 12(15):6863–6889
- Tjernström M, Leck C, Birch CE, Bottenheim JW, Brooks BJ, Brooks IM, Bäcklin L, Chang RY-W, de Leeuw G, Di Liberto L, de la Rosa S, Granath E, Graus M, Hansel A, Heintzenberg J, Held A, Hind A, Johnston P, Knulst J, Martin M, Matrai PA, Mauritsen T, Müller M, Norris SJ, Orellana MV, Orsini DA, Paatero J, Persson POG, Gao Q, Rauschenberg C, Ristovski Z, Sedlar J, Shupe MD, Sierau B, Sirevaag A, Sjogren S, Stetzer O, Swietlicki E, Szczodrak M, Vaattovaara P, Wahlberg N, Westberg M, Wheeler CR (2014)

- The Arctic Summer Cloud Ocean Study (ASCOS): overview and experimental design. *Atmos Chem Phys* 14(6):2823–2869
- Tjernström M, Shupe MD, Brooks IM, Persson POG, Prytherch J, Salisbury DJ, Sedlar J, Achtert P, Brooks BJ, Johnston PE, Sotiropoulou G, Wolfe D (2015) Warm-air advection, air mass transformation and fog causes rapid ice melt. *Geophys Res Lett* 42(13):5594–5602
- Uttal T, Curry JA, Mcphee MG, Perovich DK, Moritz RE, Maslanik JA, Guest PS, Stern HL, Moore JA, Turenne R, Heiberg A, Serreze MC, Wylie DP, Persson OG, Paulson CA, Halle C, Morison JH, Wheeler PA, Makshtas A, Welch H, Shupe MD, Intrieri JM, Stamnes K, Lindsey RW, Pinkel R, Pegau WS, Stanton TP, Grenfeld TC (2002) Surface heat budget of the Arctic Ocean. *Bull Am Meteorol Soc* 83(2):255–275
- Vaisala (2002) Weather sensor FD12P user's guide. M210296en-A, Helsinki
- Vaisala (2017) Radiosonde RS92 : <http://www.vaisala.com/en/products-/soundingsystemsandradiosondes/radiosondes/Pages/RS92.aspx>. Accessed 28 May 2017
- Van Tricht K, Lhermitte S, Lenaerts JT, Gorodetskaya IV, L'Ecuyer TS, Noël B, van den Broeke MR, Turner DD, Van Lipzig NP (2016) Clouds enhance Greenland ice sheet meltwater runoff. *Nat Commun*. <https://doi.org/10.1038/ncomms10266>
- Vavrus S, Holland MM, Bailey DA (2011) Changes in Arctic clouds during intervals of rapid sea ice loss. *Clim Dynam* 36(7–8):1475–1489
- Vinje T (2001) Fram Strait ice fluxes and atmospheric circulation: 1950–2000. *J Clim* 14(16):3508–3517
- Welch RM, Wielicki BA (1986) The stratocumulus nature of fog. *J Appl Meteorol Clim* 25(2):101–111
- Wood R (2012) Stratocumulus clouds. *Mon Weather Rev* 140(8):2373–2423
- World Meteorological Organization (WMO) (1995) Manual on codes, volume I.1: part A—alphanumeric codes. WMO-No. 306, Geneva
- World Meteorological Organization (WMO) (2017) International cloud atlas (2017 edn). <https://cloudatlas.wmo.int/>. Accessed 1 Feb 2018
- Zhang YH, Seidel DJ (2011) Challenges in estimating trends in Arctic surface-based inversions from radiosonde data. *Geophys Res Lett*. <https://doi.org/10.1029/2011GL048728>
- Zhang T, Stamnes K, Bowling SA (1996) Impact of clouds on surface radiative fluxes and snowmelt in the Arctic and Subarctic. *J Clim* 9(9):2110–2123
- Zhang SP, Xie SP, Liu QY, Yang YQ, Wang XG, Ren ZP (2009) Seasonal variations of Yellow Sea fog: observations and mechanisms. *J Clim* 22(24):6758–6772
- Zhang Y, Seidel DJ, Golaz JC, Deser C, Tomas RA (2011) Climatological characteristics of Arctic and Antarctic surface-based inversions. *J Clim* 24(19):5167–5186